Biophysical Journal
Article

Biophysical Society

Probing the Structural Dynamics of the NMDA Receptor Activation by Coarse-Grained Modeling

Wenjun Zheng,[1,*] Han Wen,[1] Gary J. Iacobucci,[2] and Gabriela K. Popescu[2]
[1]Department of Physics and [2]Department of Biochemistry, State University of New York at Buffalo, Buffalo, New York

ABSTRACT N-Methyl-D-aspartate (NMDA) receptors are glutamate-gated excitatory channels that play essential roles in brain functions. High-resolution structures have been solved for an allosterically inhibited and agonist-bound form of a functional NMDA receptor; however, other key functional states (particularly the active open-channel state) were only resolved at moderate resolutions by cryo-electron microscopy (cryo-EM). To decrypt the mechanism of the NMDA receptor activation, structural modeling is essential to provide presently missing information about structural dynamics. We performed systematic coarse-grained modeling using an elastic network model and related modeling/analysis tools (e.g., normal mode analysis, flexibility and hotspot analysis, cryo-EM flexible fitting, and transition pathway modeling) based on an active-state cryo-EM map. We observed extensive conformational changes that allosterically couple the extracellular regulatory and agonist-binding domains to the pore-forming trans-membrane domain (TMD), and validated these, to our knowledge, new observations against known mutational and functional studies. Our results predict two key modes of collective motions featuring shearing/twisting of the extracellular domains relative to the TMD, reveal subunit-specific flexibility profiles, and identify functional hotspot residues at key domain-domain interfaces. Finally, by examining the conformational transition pathway between the allosterically inhibited form and the active form, we predict a discrete sequence of domain motions, which propagate from the extracellular domains to the TMD. In summary, our results offer rich structural and dynamic information, which is consistent with the literature on structure-function relationships in NMDA receptors, and will guide in-depth studies on the activation dynamics of this important neurotransmitter receptor.

INTRODUCTION

N-Methyl-D-aspartate (NMDA) receptors are a family of glutamate-gated cation channels critically involved in brain development and function, which include GluN1, GluN2A-D, and GluN3A-B subunits (1), and are related to the other two families of ionotropic glutamate receptors, AMPA (GluA1–4) and kainate (GluK1–5) receptors. NMDA receptors assemble as heterotetramers composed of two GluN1-GluN2 heterodimers, and become active only after binding the obligatory coagonists glycine (in GluN1) and glutamate (in GluN2) (2–4) and relief of magnesium block by membrane depolarization (5,6). Unlike the AMPA/kainate receptors, the NMDA receptors have slow kinetics, a feature essential to the physiology of central excitatory synapses (1). Mutations in NMDA receptors are linked to several neurological diseases, such as Alzheimer's disease, depression, stroke, epilepsy, and schizophrenia (7).

The architecture of NMDA receptors features three distinct layers of quasi-independent domains (Fig. 1, *a–d*): most externally, four amino-terminal domains (ATDs) form two heterodimers (denoted "AB" and "CD", Fig. 1 *e*); proximal to the membrane, four ligand-binding domains (LBDs) form two heterodimers (denoted "AD" and "CB"; Fig. 1 *f*), below which is a tetrameric transmembrane domain (TMD) (Fig. 1 *g*). The two bilobed ATDs, each with R1 and R2 lobes, bind allosteric modulators (8) and regulate channel open probability and kinetics (9–11). The two bilobed LBDs, each with D1 and D2 lobes, bind agonists and can undergo closure of the D1-D2 cleft to permit channel opening (12). The TMD consists of four hydrophobic helical segments (M1–M4) in each subunit, and the C-terminal part of M3 and the N-terminal part of M4 line the cation-permeable pore (13,14). Recently, two high-resolution crystal structures of functional heterotetrameric GluN1/GluN2B receptors were solved with bound agonists and allosteric inhibitors (ifenprodil or Ro 25-6981) (15,16), which captured an allosterically inhibited state with the GluN2B ATD in a closed conformation (15–18). Similar high-resolution structures for resting and active

Submitted February 28, 2017, and accepted for publication April 27, 2017.
*Correspondence: wjzheng@buffalo.edu
Editor: Vasanthi Jayaraman.
http://dx.doi.org/10.1016/j.bpj.2017.04.043

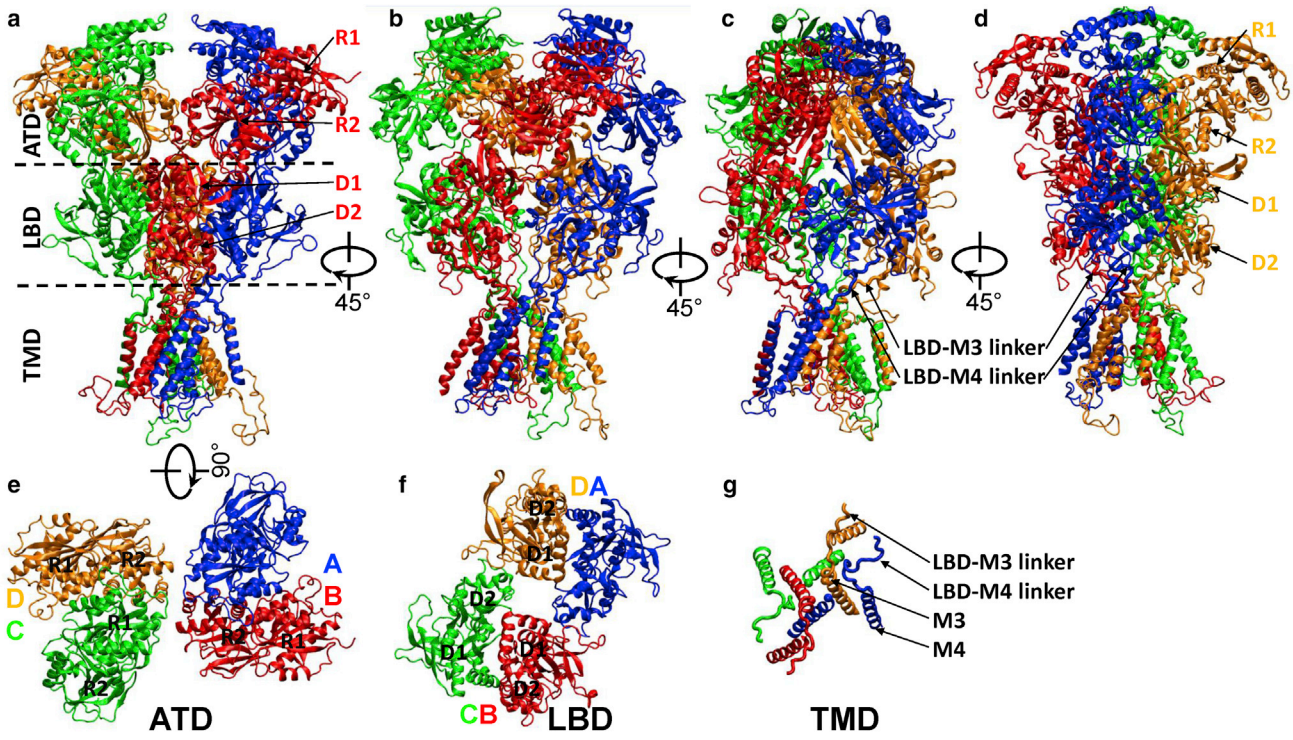

FIGURE 1 Architecture of GluN1/GluN2A receptor. (*a–d*) Shown here are different side views with the receptor rotated in increments of 45°. (*e–g*) Shown here is the top view of the ATD layer (R1 and R2), the LBD layer (D1 and D2), and the partial TMD (M3, M4, and associated linkers), respectively. The two GluN2A subunits are colored red (chain *B*) and orange (chain *D*), and the two GluN1 subunits are colored blue (chain *A*) and green (chain *C*). To see this figure in color, go online.

states are presently unavailable and the structural mechanism of receptor activation remains obscure. However, two recent cryo-EM studies (19,20) visualized functional GluN1/GluN2B receptors at sub-/near-nanometer resolutions. Importantly, these studies captured active and antagonist-bound states, offering additional information on conformational changes associated with activation (20) and antagonist inhibition (19). Although adequate resolution in the extracellular layers permitted modeling the active-state conformations for these domains (20), insufficient resolution in the TMD still obscures how conformational changes in the extracellular domains translate into pore opening during receptor activation.

Molecular dynamics (MD) is the method of choice for predicting protein dynamics under physiological conditions at atomic resolution (21). It was previously used to study agonist binding in the LBD (22,23) and the gating dynamics of several ion channels (24–28), including NMDA receptors (29). MD simulation nicely complements experimental dynamic measurements of NMDA receptors (30–34). Despite fast-growing computing power, MD simulation is still highly expensive, especially for large biomolecular complexes in explicit solvent. Typical speeds of MD simulation on a single computer node equipped with a graphics processing unit are $\leq$10 ns per day for a system of 10^5–10^6 atoms, although much higher speeds (e.g., several microseconds per day) can be reached on a massively parallelized or special-purpose supercomputer (35). Therefore, MD simulation cannot presently access the milliseconds-to-seconds timescales physiologically relevant to macromolecular complexes such as a functional NMDA receptor (with 10^5–10^6 atoms including solvent and lipids).

Coarse-grained modeling methods with reduced protein representations (e.g., one bead per amino acid residue) and simplified energy functions (e.g., harmonic potential) (36,37) promise to overcome these limitations. The elastic network model (ENM), a popular coarse-grained model, connects nearby C_α atoms of amino acids with harmonic springs (38–40). Despite its simplicity, the normal mode analysis (NMA) of ENM can yield low-frequency modes of collective domain motions, which often capture conformational changes observed between experimentally solved protein conformations (41). Numerous studies have established ENM as a useful and efficient means to probe structural dynamics of large biomolecular complexes, including glutamate receptors (42,43) and other ion channels (44–46), with virtually no limit in timescale or system size (see reviews (47,48)).

In this study, we used a series of ENM-based modeling/analysis tools to gain detailed insights into the structural dynamics of the NMDA receptor activation. Results from cryo-electron microscopy (cryo-EM) flexible fitting revealed extensive conformational changes that allosterically couple the extracellular ATD/LBD to the TMD to produce

an open pore conformation. Results from NMA predicted two key modes of collective motions involving the ATD, the LBD, and the TMD; revealed distinct subunit-specific flexibility; and identified functional hotspot residues at key interdomain interfaces. Based on modeling results for the conformational transition pathway from the allosterically inhibited state to the active state, we propose a distinct sequence of domain motions that propagate from the ATD to the TMD via the LBD. The rich structural and dynamic information afforded by our modeling results is consistent with known mutational and functional studies from the literature (Table 1), and represents a valuable guide for future in-depth studies.

MATERIALS AND METHODS

Homology modeling of the GluN1/GluN2A receptor

The structural models of rat GluN1/GluN2A receptor were built by the SWISS MODEL server (49) using the *Rattus norvegicus* and *Xenopus laevis* GluN1/GluN2B crystal structures (PDB: 4PE5 and 4TLM) as templates. We chose these template structures because they are the highest-resolution structures for functional tetrameric NMDA receptors currently available in the Protein Data Bank. The target GluN1 and GluN2A sequences of *R. norvegicus* were obtained from the UniProt/Swiss-Prot database (50) (access IDs: P35439 and Q00959, respectively). The use of homology modeling is appropriate because of the high sequence similarity between the target sequences and the templates (72% identity between rat GluN2A and rat GluN2B, 70% identity between rat GluN2A and *X. laevis* GluN2B, and 89% identity between rat GluN1 and *X. laevis* GluN1). The stereochemistry of the homology models was regularized using a short energy minimization with the GROMOS 96 force field (49). We used the 4PE5-based model in this study, which includes chain A (residue number 25–829 of GluN1), chain B (residue number 29–839 of GluN2A), chain C (residue number 25–832 of GluN1), and chain D (residue number 31–836 of GluN2A). The quality of this homology model was assessed by the following QMEAN scores (49): 0.69 for chain A, 0.68 for chain B, 0.69 for chain C, and 0.65 for chain D. The following missing loops were added by the SWISS MODEL server using both backbone libraries and de novo loop-building procedures (49): H53-K57, P95-F102, T442-H449, F583-S604, S617-G622, L657-R663, and S802-L808 in chain A; V440-G449, R539-F549, S569-T600, N615-K628, and N802-G819 in chain B; P95-F102, T442-P444, S549-S553, F583-S604, and S617-G633 in chain C; V440-M450, S540-A548, I567-T600, N614-K628, and N802-N805 in chain D. Most added loops are relatively short and not expected to significantly alter the global dynamics analyzed by the coarse-grained modeling. However, two long dangling loops in the TMD (F583-S604 in chain C and I567-T600 in chain D) may contribute to unrealistically large local fluctuations and spurious hotspot residues (Table 2). Because coarse-grained modeling of structural dynamics is dictated by the global shape and domain connectivity, which are not sensitive to small errors in local structures, these homology models are adequate for the purpose of this study.

ENM and NMA

In an ENM, a protein is represented as a network of coarse-grained beads corresponding to the C_α atoms of amino acid residues. Harmonic springs link all pairs of beads within a cutoff distance R_c of 25 Å (51). A large R_c ensures good local connectivity of the ENM to avoid an unwanted tip effect (52).

The ENM potential energy is the following:

$$E = \frac{1}{2}\sum_{i=1}^{N}\sum_{j=1}^{i-1} k_{ij}\theta\left(R_c - d_{ij,0}\right)\left(d_{ij} - d_{ij,0}\right)^2, \qquad (1)$$

where N is the number of beads; $\theta(x)$ is the Heaviside function; and d_{ij} is the distance between bead i and j, and $d_{ij,0}$ is the value of d_{ij} as given by a reference structure. The spring constant k_{ij} is set to be $(4/d_{ij,0})^2$ for nonbonded interactions (following (51,53)) and 10 for bonded interactions (in arbitrary unit). We tested other ENM schemes (e.g., $k_{ij} \propto d_{ij,0}^{-6}$), and verified that the NMA results are insensitive to the choice of ENM schemes.

The NMA solves the following eigen equation for a Hessian matrix H, which is obtained by calculating the second derivatives of ENM potential energy (44):

$$HV_m = \lambda_m V_m, \qquad (2)$$

where λ_m and V_m represent the eigenvalue and eigenvector of mode m, respectively. After excluding six zero modes corresponding to three rotations and three translations, we number nonzero modes starting from one in the order of ascending eigenvalue.

For mode m, we use a perturbation analysis to assess how much the eigenvalue changes (represented as $\delta\lambda_m$) in response to a perturbation at a chosen residue position (54–56) (i.e., by uniformly weakening the springs connected to this position to mimic an alanine substitution). Then we average $\delta\lambda_m/\lambda_m$ over the lowest $M = 20$ modes to assess the dynamic importance of this residue position (57), as follows:

$$\langle \delta\lambda/\lambda \rangle = \frac{1}{M}\sum_{m=1}^{M} \delta\lambda_m/\lambda_m. \qquad (3)$$

TABLE 1 Distance Changes between Selected Pairs of Residues upon Activation

Residue Pair	Domain Location	Distance change (Å)	Related Functional Motion upon Activation
$S126_{N1}$-$H171_{N1}$	$R1_{N1}$-$R2_{N1}$	2	intrasubunit R1-R2 opening
$H101_{N1}$-$H171_{N1}$	$R1_{N1}$-$R2_{N1}$	3	intrasubunit R1-R2 twisting
$G200_{N1}$-$E328_{N2A}$	$R2_{N1}$-$R1_{N2A}$	5	intradimer R1-R2 opening
$A175_{N1}$-$R181_{N2A}$	$R2_{N1}$-$R2_{N2A}$	−2	intradimer R2-R2 closing
$K178_{N1}$-$S185_{N2A}$	$R2_{N1}$-$R2_{N2A}$	−3	intradimer R2-R2 closing
$Q696_{N1}$-$G784_{N2A}$	$D2_{N1}$-$D1_{N2A}$	1	intradimer D1-D2 opening
$E781_{N1}$-$N697_{N2A}$	$D1_{N1}$-$D2_{N2A}$	−2	intradimer D1-D2 closing
$Y535_{N1}$-$V783_{N2A}$	$D1_{N1}$-$D1_{N2A}$	−1	intradimer D1-D1 closing
$K669_{N2A}$-$K669_{N2A}$	LBD-M3 linkers of N2A	10	outward pulling of LBD-M3 linkers in N2A
$R671_{N1}$-$R671_{N1}$	LBD-M3 linkers of N1	0	no pulling of LBD-M3 linkers in N1
$M823_{N2A}$-$V635_{N1}$	$M4_{N2A}$-$M3_{N1}$	2	relative M3-M4 sliding

TABLE 2 Hotspot Residues in GluN1, Chains A and C and GluN2A, Chains B and D

Chain ID	Hotspot Residues
A	D170 D198 P199 G200 E294 E297 K298 E299 N300 I301 T302 S327 N491 N492 S493 I546 P547 R548 S549 D799 S800 R801 N803 A804
C	D170 D198 P199 G200 E294 L296 E297 K298 E299 N300 I301 T302 S327 N491 N492 S493 I546 P547 R548 S549 T550 L580 D581 R582 F583 S584 P585 F586 G587 R588 F589 K590 V591 N592 S593 E594 E595 E596 E597 E598 D599 L603 R625 F627 A629 R630 C744 C798 D799 S800 R801 S802 N803 A806
B	P140 D212 A213 K214 Q216 S241 E242 R244 S245 L246 G247 C399 E400 P401 D403 T543 V544 Q620 N621 F658 V659 D660
D	P140 D212 A213 K214 Q216 S241 E242 R244 S245 L246 G247 S397 D398 C399 E400 P401 D402 S545 V563 L566 I567 V568 S569 A570 I571 A572 V573 F574 V575 F576 E577 Y578 F579 S580 P581 V582 G583 Y584 N585 R586 N587 L588 A589 K590 G591 K592 A593 P594 H595 G596 P597 S598 F599 T600 G602 K603 K628 I814 D815 N816 M817 S831 I833 T834 F835 I836

To validate ENM-based NMA, we compare each mode (i.e., mode m) with the observed structural change X_{obs} between two superimposed protein structures by calculating the following overlap (58):

$$I_m = X_{\text{obs}} \cdot V_m / |X_{\text{obs}}|, \quad (4)$$

where $|I_m|$ varies between 0 and 1 with higher value meaning greater similarity. I_m^2 gives the fractional contribution of mode m to X_{obs}. The cumulative squared overlap $C_M = \sum_{m=1}^{M} I_m^2$ gives the fractional contribution of the lowest $M = 20$ modes to X_{obs} (58).

To assess the flexibility profile at individual residue positions, as described by the lowest $M = 20$ modes, we define the following cumulative flexibility (CF) (46,57):

$$CF_n = \sqrt{\sum_{m=1}^{M} \left(|V_{m,nx}|^2 + |V_{m,ny}|^2 + |V_{m,nz}|^2 \right)}, \quad (5)$$

where $V_{m,nx}$, $V_{m,ny}$, and $V_{m,nz}$ are the x, y, and z component of mode m's eigenvector at residue position n.

Flexible fitting of cryo-EM map

We previously developed a coarse-grained method (named "EMFF") based on a modified form of ENM to flexibly fit a given initial Cα-only structure into a target cryo-EM density map (available at http://enm.lobos.nih.gov/emff/start_emff.html). It allows us to model the conformational changes from the initial state to the target state at residue-level resolution (59) as follows. We first fitted the initial structure rigidly into the target cryo-EM map using the colores command of the SITUS program (http://situs.biomachina.org/). Then we ran flexible fitting to iteratively generate a series of 10 conformations with increasing root mean squared deviation from the initial structure and gradually improving fitting to the given cryo-EM map as assessed by the cross-correlation coefficient (59). We terminated the flexible fitting upon saturation of the cross-correlation coefficient. Here we applied EMFF to the active-state cryo-EM map of the NMDA receptor (EMDB: 3352), starting from a homology model of the GluN1/GluN2A receptor in an allosterically inhibited and agonist-bound state (see above). To ensure the robustness of our modeling, we performed two separate flexible fittings starting from two distinct homology models (see above) and only reported structural changes common to both flexibly fitted models.

Coarse-grained transition pathway modeling

We previously developed an interpolated ENM (iENM) protocol to construct a transition pathway (i.e., a series of C_α-only intermediate conformations) between an initial and an end protein conformation by solving the saddle points of a double-well potential built from these two conformations (60) (available at http://enm.lobos.nih.gov/start_ienm.html). Here we applied this method to the conformational transition from the allosterically inhibited to the active form (as modeled by EMFF, see above). Based on the iENM-predicted transition pathway, we determined the motional order of various domains by calculating and comparing the reaction coordinates for these domains (denoted RC_S for domain S; for details, see (61)). RC_S varies from 0 to 1 as the transition advances from the initial to the end conformation. For two domains S and S′, if $RC_S < RC_{S'}$ along the pathway, we infer that the motion of S′ precedes that of S. Here we plot $RC_S - RC_{\text{all}}$ as a function of RC_{all} (i.e., RC of all residues) to track the evolution of RC_S along the transition pathway.

RESULTS AND DISCUSSION

Cryo-EM-based flexible fitting reveals conformational changes toward an active state of the NMDA receptor

To determine the structural events that represent NMDA receptor activation, it is critical to develop a structural model for the active open-channel state. Despite subnanometer resolution (6.8 Å), the cryo-EM map of the active state only allowed modeling via rigid fitting of the extracellular ATD/LBD domains (20), whereas the TMD and key LBD-TMD linkers could not be resolved (20). To complete the active-state conformation of a functional NMDA receptor with residue-level resolution, we used a coarse-grained method (59) to flexibly fit an allosterically inhibited structure of rat GluN1/GluN2A receptor into the active-state cryo-EM map (EMDB: 3352). The initial GluN1/GluN2A models were built by homology modeling (see Materials and Methods) based on the x-ray structures of GluN1/GluN2B receptor (PDB: 4PE5 and 4TLM). Relative to other cryo-EM-based flexible fitting methods (62,63), our coarse-grained method (59) is more efficient and therefore better suited for modeling large protein complexes (45). During flexible fitting, we generated a series of Cα-only models (Movie S1) that progressively deviate from the initial structure, with gradually increasing root mean squared deviation to 6.5 Å and improved fitting to the given cryo-EM map (with the cross-correlation coefficient increasing from 0.42 to 0.85), while maintaining the global/local structural integrity (59). Using flexible fitting, we obtained very similar models for 4PE5 and 4TLM, and subsequently only analyzed the flexibly fitted model from 4PE5. Below we describe the extensive conformational changes revealed by flexible fitting from the allosterically inhibited state to the active state (Fig. 2).

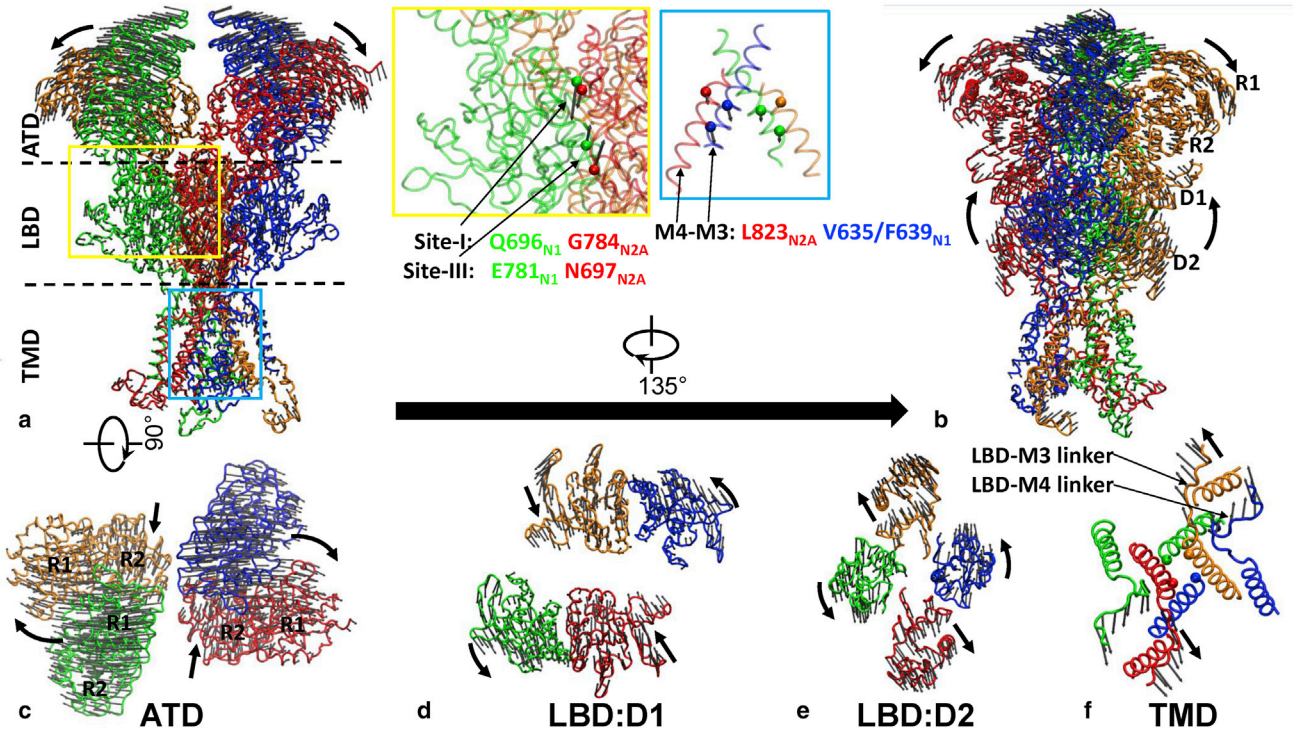

FIGURE 2 Shown here are the conformational changes from the allosterically inhibited state to the active state modeled by cryo-EM flexible fitting and illustrated by a vector plot, where thin arrows represent the three-dimensional components of the conformational changes at individual residues (i.e., the length of an *arrow* is proportional to the magnitude of movement of a given residue). The vector plot was produced using the Normal Mode Wizard plugin of the VMD program (89). (*a* and *b*) Shown here are two side views with the receptor rotated by 135°. The two insets show specific motions at LBD site I, site III, and the interface between M4 of GluN2A and M3 of GluN1. (*c–f*) Shown here is the top view of the ATD layer (R1 and R2), the LBD D1 layer, the LBD D2 layer, and the partial TMD (M3, M4, and associated linkers), respectively. The two GluN2A subunits are colored red (chain *B*) and orange (chain *D*), and the two GluN1 subunits are colored blue (chain *A*) and green (chain *C*). Domain motions are labeled by thick arrows. To see this figure in color, go online.

In the ATD layer, which encompasses four R1/R2 lobes (Fig. 2 *c*), we observed large and small domain motions between and within the ATD heterodimers, respectively, as quantified by distance changes between the centroids of R1/R2 lobes (see below). Between the two ATD heterodimers, the diagonally opposing R1/R2 lobes undergo distinct motions in GluN1 and GluN2A: the R1 lobes move apart by ∼19 and ∼7 Å in GluN1 and GluN2A, respectively, whereas the R2 lobes move apart by ∼7 Å in GluN1 and closer by ∼5 Å in GluN2A, respectively (Fig. 2 *c*). In each ATD heterodimer, the R1 and R2 lobes move closer by ∼2 and ∼4 Å, respectively. The intradimer closure of R2 lobes as observed here compares well with movements reported based on superimposing the apo ATD tetramer structure to an ifenprodil-bound ATD dimer structure (20). In each ATD subunit, the R1-R2 cleft opens by ∼2 and ∼1 Å in GluN2A and GluN1, respectively, as observed in an apo structure of ATD tetramer (20). The above distinct domain motions between GluN1 and GluN2A may underscore their different roles in the allosteric modulation of channel activity (11,64).

At the ATD-LBD interface, we observed intra- and intersubunit domain motions between the ATD R2 lobes and the LBD D1 lobes (Fig. 2, *c* and *d*). Within each subunit, R2 and D1 move apart by ∼3 and ∼1 Å in GluN1 and GluN2A, respectively. In contrast, between adjacent subunits, the R2 of GluN2A moves closer to the D1 of GluN1 by ∼1 Å, whereas the R2 of GluN1 moves away from the D1 of GluN2A by ∼5 Å. These distinct motions may underscore subunit-specific coupling between the ATD and the LBD layers, which was thought to control how agonist binding leads to channel opening (65). The smaller motions of the GluN2A R2 suggest tighter ATD-LBD coupling in GluN2A, consistent with a strong regulatory role reported for the GluN2A ATD (11).

In the LBD layer, which encompasses four D1/D2 lobes (Fig. 2, *d* and *e*), we also observed subunit-specific domain motions. The two LBDs of GluN2A rotate in opposite directions (Fig. 2 *b*, *side view*), such that their D1 and D2 lobes move closer by ∼5 Å and apart by ∼7 Å, respectively (Fig. 2, *d* and *e*). In contrast, the two LBDs of GluN1 undergo concerted counterclockwise rotations (Fig. 2, *d* and *e*, *top view*), resulting in only ∼1 and ∼2 Å separation between the D1 and D2 lobes, respectively. Similar counterclockwise rotations of LBDs were observed by cryo-EM during the activation of AMPA receptor (66). These subunit-specific D2 motions may lead to asymmetric channel opening in the TMD of NMDA receptor as proposed previously (29). Additionally, we observed partial opening of the

LBD cleft in both GluN1 and GluN2A, indicated by ~3 Å increase in $\xi 2$ and <1 Å change in $\xi 1$, where $\xi 1$ and $\xi 2$ are two distances between specific sites in D1 and D2 that measure the LBD cleft openness (following (23); see (67) for the original definition). The observed uneven changes in $\xi 1$ and $\xi 2$ are consistent with the calculated free-energy landscape of LBD (23) featuring low-energy basins elongated along the $\xi 2$ direction. In the predicted active-state conformation, the LBD cleft is more open in GluN2A than in GluN1 (with $\xi 2$ larger by 3 Å), consistent with the proposal that the GluN2 ligand glutamate, but not the GluN1 ligand glycine, activates NMDA receptors with submaximal efficacy (68).

At the LBD-TMD interface, three linkers connect the D2 lobe to the three transmembrane helices M1, M3, and M4. Notably, the LBD-M3 linker of GluN2A and the LBD-M4 linker of GluN1 are oriented parallel to the membrane (Fig. 2 *f*), suggesting that they may contribute to channel opening by exerting outward tension on the M3 and M4 helices. This suggestion is supported by the observation that increased separation between the D2 lobes of GluN2A correlates with outward movement of the two LBD-M3 linkers, resulting in ~2 Å separation of the uppermost portion of M3, which encompasses the activation gate (69) (Fig. 2 *f*). Likewise, the rotation of GluN1 D2 lobes may pull apart the two LBD-M4 linkers and favor concerted outward movement of GluN1 M4 and adjacent GluN2A M3 (Fig. 2 *f*). These observations are consistent with the view that the energy of agonist binding serves to open the activation gate by prompting concerted outward motions of the M3 and M4 helices (13).

In summary, our modeling study revealed subunit-specific domain motions during activation of the NMDA receptor, as supported by a wealth of previous experimental observations (see below). In GluN2 subunits, the conformational changes we observed are consistent with the general model of ionotropic receptor activation via the LBD-M3 linkers (70). We also observed additional motions pertinent to activation, which occur via the GluN1 LBD-M4 linkers due to simultaneous rotations of the GluN1 LBDs. The limited resolution of current cryo-EM maps in the transmembrane regions prevents us from obtaining insights into possible rearrangements deeper in the TMD (e.g., near the selectivity filter (71)). Therefore, whether and how motions in the M3 and M4 helices couple to the internal sites remains unclear (13). Given, to our knowledge, the novelty of this modeling study, we next sought to validate our modeling results comprehensively against the experimental literature of NMDA receptors.

Validation of modeling in comparison with experimental literature

ATD layer

To investigate the roles of closing and untwisting motions of R1 and R2 lobes in allosteric inhibition, a previous study (64) introduced three Cys cross linkers: between $S126_{N1}$ and $H171_{N1}$, between $H101_{N1}$ and $H171_{N1}$, and between $G200_{N1}$ and $I329_{N2B}$ (corresponding to $E328_{N2A}$). These perturbations substantially reduced channel activity presumably by locking ATD in a closed-cleft conformation, an untwisted conformation, and an $R2_{N1}$-$R1_{N2A}$ closed conformation, respectively. Consistent with these findings, our modeling showed that during activation the $S126_{N1}$-$H171_{N1}$ distance increases by ~2 Å, the $H101_{N1}$-$H171_{N1}$ distance increases by ~3 Å, and the $G200_{N1}$-$E328_{N2A}$ distance increases by ~5 Å. Therefore, by impeding these specific R1-R2 motions, binding of allosteric inhibitors or cross linking would inhibit channel activation. A recent study introduced two Cys cross linkers (20): one between $A175_{N1b}$ and $Q180_{N2B}$ (corresponding to $A175_{N1}$ and $R181_{N2A}$), and another between $K178_{N1b}$ and $N184_{N2B}$ (corresponding to $K178_{N1}$ and $S185_{N2A}$). These linkers were found to trap the receptor in an activated R2-R2 closed conformation with three-to-fourfold potentiation of the current. In agreement with these findings, our modeling showed that during activation the $A175_{N1}$-$R181_{N2A}$ and $K178_{N1}$-$S185_{N2A}$ C_α-C_α distances decrease by 2–3 Å to ~14 Å, which are compatible with the S-S linker length of ~10 Å.

LBD layer

In a recent mutagenesis and single-channel activity study, we probed the role of putative interactions at the GluN1/GluN2A interface in the LBD layer in receptor activation (72). Previous structural studies had identified two class-specific LBD sites unique to the NMDA receptors (12): site I involves contacts between $Q696_{N1}$ and $G784_{N2A}$, and site III involves contacts between $N693_{N2A}$/$N697_{N2A}$ and $E781_{N1}$. The Q696A substitution in GluN1, intended to abolish a site-I interaction, had little effect on channel activity (72). Consistent with this finding, our modeling indicates that during activation both $Q696_{N1}$ and $G784_{N2A}$ move downward with their distance increasing by ~1 Å (from 8 to 9 Å; see Fig. 2 *a*, *inset*). Therefore, the $Q696_{N1}$-$G784_{N2A}$ interaction is unlikely to form in the active state, so its loss will not destabilize the active state to compromise activation. In contrast, the double substitution N693A/N697A in GluN2A, intended to abolish site-III interactions, lowered channel open probability substantially (72). Consistent with this finding, our modeling predicts that both $E781_{N1}$ and $N697_{N2A}$ move upward with their distance decreasing by ~2 Å (from 8 to 6 Å; see Fig. 2 *a*, *inset*). Therefore, the $E781_{N1}$-$N697_{N2A}$ interaction is more likely to form in the active state relative to the closed state, so its disruption may destabilize the active state and reduce open probability.

Recent studies have delineated structural changes upon binding of positive allosteric modulators and negative allosteric modulators at the D1-D1 interfaces in each GluN1/GluN2A heterodimer (73–75). Positive allosteric modulator binding causes a slight decrease (~1 Å) in separation between $Y535_{N1}$ and $V783_{N2A}$ with the $Y535_{N1}$ side chain

pointing toward $V783_{N2A}$ (73,74), whereas the negative allosteric modulator-bound and apo structures are similar, with the $Y535_{N1}$ side chain pointing away from $V783_{N2A}$ (75) (see Fig. 2 of (73)). Consistent with these findings, our modeling indicates $Y535_{N1}$ and $V783_{N2A}$ move closer by ~1 Å upon activation, which supports a common mechanism of channel activation and positive allosteric modulation via tightening of the D1-D1 intradimer interface.

Taken together, our modeling supports the pivotal role of the LBD heterodimer interface and its moderate conformational changes in the activation and modulation of the NMDA receptor activity (76).

LBD-TMD interface

To evaluate conformational changes in the LBD-M3 linkers during activation, we measured relevant distances across two GluN1 and GluN2A subunits. We found that the distance between two GluN2A linkers, as measured between $K669_{N2A}$, increases substantially from 69 to 79 Å, whereas the distance between two GluN1 linkers, measured between corresponding residues $R671_{N1}$, remains unchanged (~30 Å). These values match well with the distances measured in two known structures of active-state AMPA receptors. In one structure, the distances between the corresponding GluA2 residues (S640) are 30 Å between A and C, and 77 Å between B and D subunits (PDB: 4UQ6) (66). In another structure, the corresponding distances are 30 and 75 Å, respectively (PDB: 4U1Y) (77). This close match between our model of NMDA receptor and those observed experimentally in AMPA receptors suggest similar asymmetric structure in the LBD-M3 linkers upon activation in these two families of glutamate receptors.

TMD layer

In all known structures of glutamate receptors, the TMD has the least structural detail. Using functional measurements, Ren et al. (78) identified four pairs of residues in this region whose interactions control NMDA receptor activation and the inhibitory action of ethanol. These pairs reside at the M3-M4 interfaces between GluN1 and GluN2 subunits: $G638_{N1}$/$M823_{N2A}$, $F639_{N1}$/$L824_{N2A}$, $M818_{N1}$/$F636_{N2A}$, and $L819_{N1}$/$F637_{N2A}$. Among them, $F637_{N2A}$ (79) and $M823_{N2A}$ (80) strongly regulate channel activation as revealed by mutational and functional measurements, with $M823_{N2A}$ of M4 likely forming hydrophobic interactions with M3 to stabilize the channel in the closed and/or desensitized states, but not in the active state (80). Our model is consistent with this conclusion. We found that $M823_{N2A}$ of M4 interacts with $V635_{N1}$ and $F639_{N1}$ of M3 (Fig. 2 *a*, *inset*), but $M818_{N1}$/$L819_{N1}$ of M4 do not contact $F636_{N2A}$/$F637_{N2A}$ of M3. The distances between $M823_{N2A}$ and $V635_{N1}$/$F639_{N1}$ increase by 1–2 Å upon activation, due to a relative downward motion between $M823_{N2A}$ and $V635_{N1}$/$F639_{N1}$ (Fig. 2 *a*, *inset*). Therefore, our modeling suggests the above hydrophobic interactions between M3 and M4 may specifically stabilize the closed but not the active state, and therefore mutations that abolish these interactions will reduce inhibition by allosteric modulators (such as ethanol) acting at this site, and favor activation as observed experimentally (78,80).

Together, the positive agreement between our structural model and published functional data gave us confidence in the quality of our predicted conformational changes, especially in the LBD intradimer interfaces and the TMD M3-M4 interfaces, where we predicted relatively small functional motions during activation (see Table 1).

NMA predicts key domain motions, flexibility profiles, and functional hotspots

Next, we used the ENM-based NMA to identify prevalent motional modes that may initiate the activation transition of NMDA receptor from the allosterically inhibited state to the active state (as modeled above). Based on the allosterically inhibited structure of rat GluN1/GluN2A receptor (modeled from a GluN1/GluN2B structure, see Materials and Methods), we constructed a C_α-only ENM by linking all pairs of residues within a cutoff distance with harmonic springs (see Materials and Methods). Then we performed NMA to obtain a spectrum of a total of 9690 modes, and focused on the lowest 20 modes, each describing a specific pattern of collective motions that involve the ATD/LBD/TMD domains of NMDA receptor.

For validation of the lowest 20 modes, we evaluated how well they collectively capture the observed conformational changes from the allosterically inhibited structure to the active-state structural model predicted by cryo-EM flexible fitting (Fig. 2). We calculated the overlap between each mode and the observed conformational changes, and the cumulative squared overlap of the lowest 20 modes (see Materials and Methods). We found that the lowest 20 modes capture ~62% of the above conformational changes, with modes 4 and 8 contributing the most (Fig. 3 *a*; overlap ~0.4). Mode 4 features an opening/shearing motion between the two ATD heterodimers, resulting in larger separation between the GluN2A ATDs than between the GluN1 ATDs, along with a counterclockwise rotation of the LBDs and a clockwise rotation of the TMD (Fig. 4, *a–d*). In contrast, mode 8 features a different opening/shearing motion between the two ATD heterodimers, resulting in larger separation between the GluN1 ATDs than between the GluN2A ATDs, accompanied by a counterclockwise rotation of the LBDs and a clockwise rotation of the TMD (Fig. 4, *e–h*). Taken together, these two modes partially capture the observed opening of ATD heterodimers and the counterclockwise rotation of LBDs in GluN1 upon activation (Fig. 2, *a* and *c–e*). However, we did not observe the other domain motions involved in activation (e.g., the closing/opening of D1/D2 in GluN2A and the outward motion of the LBD-M3 linkers in GluN2A; see Fig. 2, *d–f*),

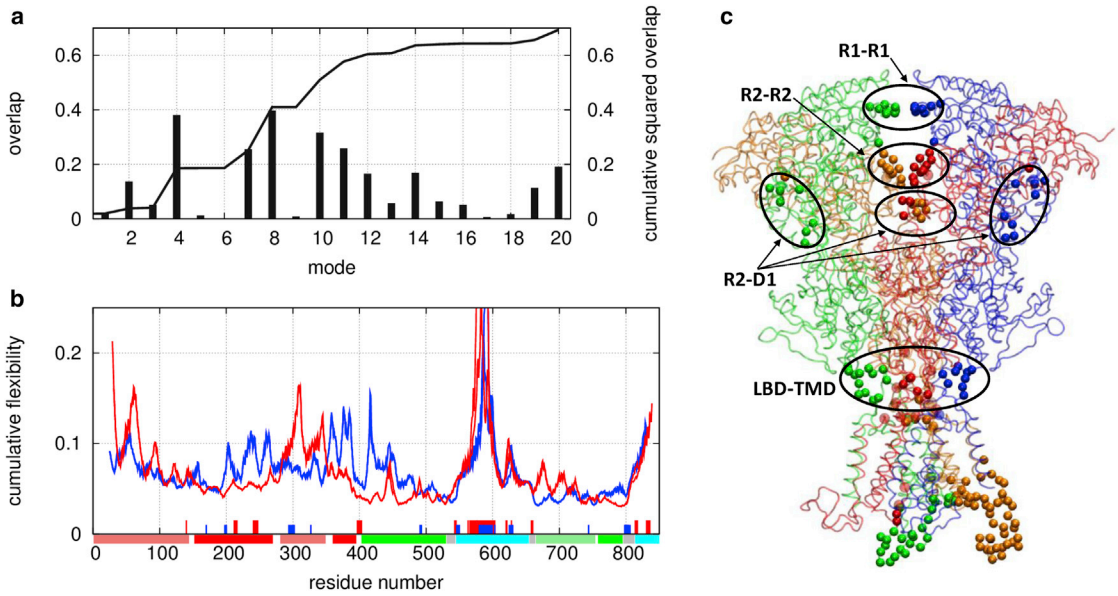

FIGURE 3 Results of ENM-based NMA. (*a*) Shown here are the overlap and the cumulative squared overlap between the activation conformational changes (see Fig. 2) and the lowest 20 modes, with modes 4 and 8 having the highest overlap. (*b*) Shown here is the cumulative flexibility profile for GluN1 (*blue curve*) and GluN2A (*red curve*), where hotspot residues are located by short dashes (*blue* for GluN1 and *red* for GluN2A), and the residue ranges for various domains are marked by horizontal bars colored as follows: R1 (*light red*), R2 (*red*), D1 (*green*), D2 (*light green*), TMD (*cyan*), and LBD-TMD linkers (*gray*). (*c*). Given here is a structural view of the hotspot residues (represented as *solid spheres* colored by *chains*: *A* (*blue*), *B* (*red*), *C* (*green*), and *D* (*orange*)), which are clustered at domain-domain interfaces (R1-R1, R2-R2, R2-D1, and LBD-TMD, see *circled regions*), and colocalize with disease mutation sites (represented as *transparent spheres* colored by *chains*). See Tables 2 and 3 for details of the hotspot residues and the mutation sites. To see this figure in color, go online.

implying that these motions are not favored by the allosterically inhibited structure and may occur later during the activation transition (see below).

To measure the flexibility of NMDA receptor domains, we used the lowest 20 modes to calculate the cumulative flexibility (*CF*; see Materials and Methods) at individual residue positions in the allosterically inhibited structure (Fig. 3 *b*). High and low CF values correspond to high and low flexibility, respectively. The GluN1 and GluN2A subunits exhibit distinct flexibility profiles owning to their structural differences. In the ATD layer, we observed higher flexibility in GluN1 R2 and GluN2A R1 than GluN2A R2 and GluN1 R1 (Fig. 3 *b*), which is consistent with larger R2-R2 and R1-R1 separation in GluN1 and GluN2A, respectively (Fig. 2 *c*). The distinct CF profiles in the ATD of GluN1 and GluN2A may underlie their different roles in allosteric modulation (11,64). Likewise, in the LBD layer, we observed higher flexibility in GluN1 D1 and GluN2A D2 than GluN2A D1 and GluN1 D2 (Fig. 3 *b*), which is consistent with larger D1-D1 and D2-D2 separation in GluN1 and GluN2A, respectively (Fig. 2, *d* and *e*). In the TMD, we observed similar *CF* profiles in GluN1 and GluN2A, with pronounced peaks near the intracellular portions of M1 and M4 (Fig. 3 *b*). This correlates well with the fourfold symmetric TMD structure (Fig. 2 *f*). At the ATD-LBD interface, we found that GluN2A displays lower *CF* than GluN1 in both R2 and D1, suggesting tighter ATD-LBD coupling mediated by GluN2A, consistent with stronger impact of GluN2 ATD ligands in allosteric modulation. Notably, all three LBD-TMD linkers are located near *CF* minima (Fig. 3 *b*), consistent with their critical roles as hinges of interdomain motions. Overall, our *CF* analysis revealed dissimilar flexibility profiles in GluN1 and GluN2A extracellular domains consistent with their distinct structures and functional roles.

Next, we used an ENM-based perturbation analysis (see Materials and Methods) to identify a small set of hotspot residues that strongly affect the functional domain motions predicted by the NMA (Fig. 3, *b* and *c*; Table 2). To this end, we calculated for each residue position an average score $\langle \delta\lambda/\lambda \rangle$ as a measurement of its contribution to the energetics of the lowest 20 modes (see Materials and Methods). We designated residues in the top 5% of $\langle \delta\lambda/\lambda \rangle$ as likely functional hotspot residues that could energetically control the domain motions predicted by the lowest 20 modes. In GluN1, hotspot residues occur in the R1/R2 lobes of ATD, the D1/D2 lobes of LBD, the LBD-M1/M4 linkers, and the TMD (Fig. 3 *b*). In GluN2A, hotspot residues are mainly in the R2 lobe of ATD, the R2-D1 linkers, the LBD-M1/M3/M4 linkers, and the TMD (Fig. 3 *b*). Most of the hotspot residues clustered at domain-domain interfaces, e.g., intrasubunit R1-R2 and R2-D1 interfaces, intersubunit $R1_{N1}$-$R1_{N1}$, $R2_{N2A}$-$R2_{N2A}$, $R2_{N1}$-$D1_{N2A}$ and $R2_{N2A}$-$D1_{N1}$ interfaces, and LBD-TMD interfaces (Fig. 3 *c*, *circled*). Notably, some hotspot residues colocalize (within 10 Å) with disease-related mutations identified by previous studies in the

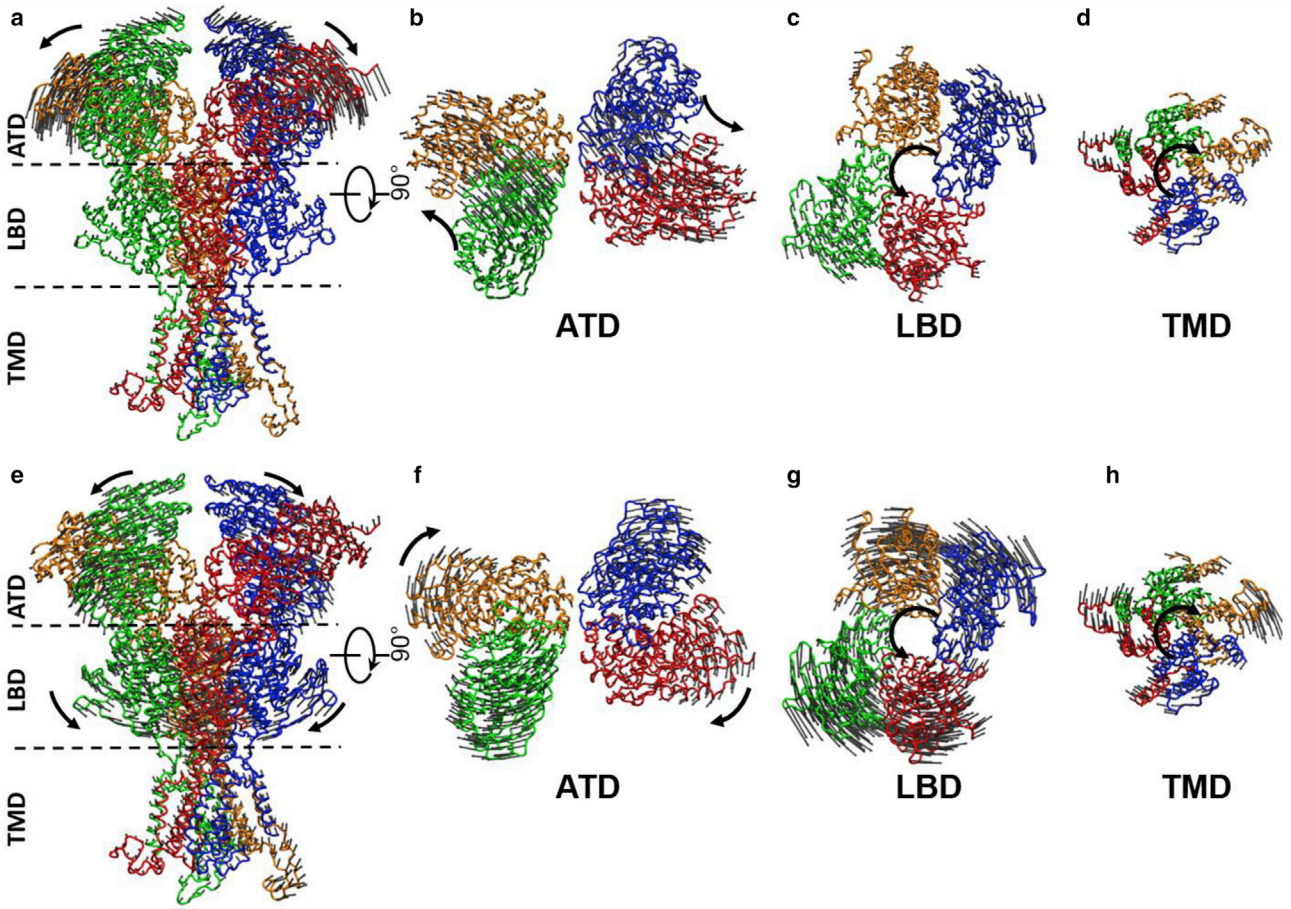

FIGURE 4 Given here are the conformational changes described by modes 4 (*a–d*) and 8 (*e–h*) as illustrated by a vector plot, where thin arrows represent the three-dimensional components of a given mode's eigenvector at individual residues (i.e., the length of an arrow is proportional to the magnitude of movement per residue as given by this eigenvector). The vector plot was produced using the Normal Mode Wizard plugin of the VMD program (89). (*a* and *e*) Given here is the same side view as Fig. 2 *a*; the remaining panels show the top view of the ATD layer, the LBD layer, and the TMD. The two GluN2A subunits are colored red (chain *B*) and orange (chain *D*), and the two GluN1 subunits are colored blue (chain *A*) and green (chain *C*). Domain rotations are labeled by thick arrows. To see this figure in color, go online.

R2 lobe of ATD, the D2 lobe of LBD, the LBD-M1/M3/M4 linkers, and the M2/M3/M4 segments of TMD (Table 3). This correspondence supports a key functional role for these hotspot residues in channel activation. In summary, our analysis uncovers hotspot sites where perturbations (e.g., mutations) may have strong effects on channel function via alteration of the functional motions, and thus provide a detailed map for future structure-function investigations.

Transition pathway modeling predicts a sequence of domain motions

Finally, to visualize the NMDA receptor activation pathway, we modeled the sequence of structural changes in GluN1/GluN2A receptor when transitioning from the allosterically inhibited structure (modeled from 4PE5, see Materials and Methods) to the active-state structure (modeled by cryo-EM flexible fitting, see above). Because NMA samples only small structural fluctuations in the vicinity of the known structures, it cannot predict intermediate conformations distant from the beginning/end structures of a transition. To overcome this limitation, we developed a coarse-grained modeling method based on an iENM (60). This method has been successfully applied to various large protein complexes to delineate sequences of domain motions during conformational transitions (44,46,58,61,81–85). When applied to the NMDA receptor, iENM predicted a plausible trajectory of intermediate conformations that connect the beginning structure to the end structure, illustrated in Movie S2.

We then applied a reaction-coordinate (RC) analysis to the predicted transition pathway (see Materials and Methods), and determined the motional order of various domains, with early and late moving domains having high and low RC values, respectively (Fig. 5). We found the domain-specific RC values decrease in the following sequence: $RC_{\mathrm{ATD}} > RC_{\mathrm{R2\text{-}D1}} > RC_{\mathrm{LBD}} > RC_{\mathrm{LBD\text{-}M3\ linker}}$. Based on this sequence, we propose that during activation, NMDA

TABLE 3 Disease Mutation Sites that Colocalize with the Predicted Hotspot Residues

Amino Acid Site	Mutation	Location in Structure	Phenotype	Reference
$D227_{N1}$	$D227H_{N1}$	intrasubunit R2-D1 and R2-R1 interface	mental retardation	224815[a] of GRIN1[b]
$P557_{N1}$	$P557R_{N1}$	LBD-M1 linker	intellectual disability	235846 of GRIN1
$G620_{N1}$	$G620R_{N1}$	M2	mental retardation	209159 of GRIN1
$A243_{N2A}$	$A243V_{N2A}$	R2-R2 interface	Rolandic epilepsy	(88)
$R539_{N2A}$	$R540H_{N2B}$	LBD-M1 linker	epileptic encephalopathy	162087 of GRIN2B[c]
$A548_{N2A}$	$A548T_{N2A}$	LBD-M1 linker	Landau-Kleffner syndrome	(88)
$P552_{N2A}$	$P552R_{N2A}$	LBD-M1 linker	epilepsy	39663 of GRIN2A[d]
$G610_{N2A}$	$G611V_{N2B}$	M2	likely pathogenic	205730 of GRIN2B
$N615_{N2A}$	$N615K_{N2A}$	M2	epilepsy	29733 of GRIN2A
$V617_{N2A}$	$V618G_{N2B}$	M2	epileptic encephalopathy	162085 of GRIN2B
$V619_{N2A}$	$V620M_{N2B}$	M2	likely pathogenic	205710 of GRIN2B
$L649_{N2A}$	$L649V_{N2A}$	M3	epilepsy	39662 of GRIN2A
$F652_{N2A}$	$F652V_{N2A}$	M3	epilepsy	88733 of GRIN2A
$E656_{N2A}$	$E657G_{N2B}$	LBD-M3 linker	likely pathogenic	234479 of GRIN2B
$I750_{N2A}$	$I751T_{N2B}$	D2 (in contact with LBD-M3 linker)	likely pathogenic	234500 of GRIN2B
$S809_{N2A}$	$S810R_{N2B}$	LBD-M4 linker	pathogenic	218471 of GRIN2B
$L812_{N2A}$	$L812M_{N2A}$	LBD-M4 linker	early onset epileptic encephalopathies	(88)
$I814_{N2A}$	$I814T_{N2A}$	LBD-M4 linker	Rolandic epilepsy	(88)
$M817_{N2A}$	$M817V_{N2A}$	LBD-M4 linker	refractory seizures	(88)
$G819_{N2A}$	$G820V_{N2B}$	M4	likely pathogenic	234635 of GRIN2B
$L824_{N2A}$	$L825V_{N2B}$	M4	autism	(88)

[a]Variation ID of the CLINVAR database (http://www.ncbi.nlm.nih.gov/clinvar).
[b]Gene name of GluN1.
[c]Gene name of GluN2B.
[d]Gene name of GluN2A.

receptor undergoes a series of domain motions, which most likely occur in the following order: intradimer ATD motions → inter- and intrasubunit R2-D1 motions → interdimer LBD motions → LBD-M3 linkers motion in GluN2A. This order is consistent with the allosteric coupling between the ATD and the LBD via the R2-D1 interfaces, and between the LBD and the TMD via the LBD-M3 linkers. In this model, the initial motions occur in ATD to release the allosteric inhibition, allowing subsequent motions in LBD to trigger activation via the LBD-M3 linkers.

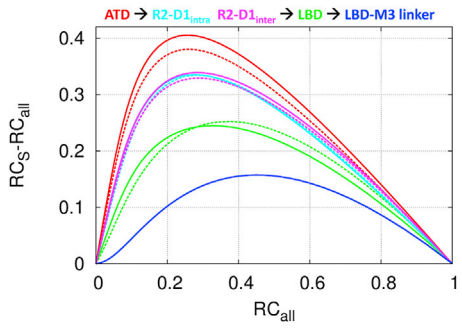

FIGURE 5 Given here is the RC analysis of transition pathway from the allosterically inhibited state to the active state as predicted by iENM. RC_S measures the motional progress for domain S, colored as follows: ATD heterodimers (*red*), LBD homodimers (*green*), R2-D1 in GluN2A (*cyan*), R2-D1 between GluN2A and GluN1 (*magenta*), and LBD-M3 linkers in GluN2A (*blue*). RC_{all} measures the motional progress for the whole receptor. $RC = 0$ and 1 at the beginning and end of the transition, respectively. The inferred motional order for the above domains is shown. To see this figure in color, go online.

We also analyzed RC for other domain motions, such as the interdimer motions of ATD, and found much lower RC (data not shown), suggesting that these motions are relatively late and less pertinent to the activation transition.

In summary, our transition pathway modeling predicted a stepwise sequence of domain motions that propagate from the ATD to the TMD via the R2-D1 interfaces, the LBD, and the LBD-M3 linkers. This is akin to the Brownian conformational wave proposed for the acetylcholine receptor activation (86). We have verified the robustness of this predicted sequence using an alternative transition pathway modeling method (see Fig. S1). Our predicted pathway is broadly consistent with present knowledge of the NMDA receptor activation sequence (ATD → LBD → TMD): the early motions in the ATD heterodimers enable their conversion from the inhibitor-bound form to the apo/activated form as observed in a crystal structure of the apo ATD tetramer (20) and validated by previous cross-linking experiments (20,64). The subsequent LBD motions enable expansion of the gating ring at the D2 level as observed structurally (16,77). Finally, the extension of the LBD-M3 linkers in N2A mechanically drive the asymmetric channel opening with the N2A subunits moving more than the N1 subunits (29,87). Future efforts to refine the coarse-grained pathway with atomic details will further advance our understanding of the activation mechanism of the NMDA receptor at the molecular level. Overall, our coarse-grained modeling results represent a springboard for detailed structure-function investigations in this critical neurotransmitter receptor and describe, to our knowledge, novel approaches to probe

function-related motions in ionotropic glutamate receptors. The lack of a realistic and accurate force field limited our coarse-grained modeling to only the general features of structural dynamics in the NMDA receptors. Specific differences in regulation and activation between different subtypes (e.g., GluN2A versus GluN2B) are beyond the scope of our coarse-grained modeling, and should be studied by all-atom modeling/simulation in the future.

SUPPORTING MATERIAL

One figure, two movies, and one data file are available at http://www.biophysj.org/biophysj/supplemental/S0006-3495(17)30459-9.

AUTHOR CONTRIBUTIONS

W.Z. and G.K.P. designed research. W.Z. and H.W. performed research. W.Z., H.W., G.J.I., and G.K.P. analyzed data. W.Z. and G.K.P. wrote the article.

ACKNOWLEDGMENTS

This study was funded in part by grants from the American Heart Association (No. 14GRNT18980033) and National Science Foundation (No. 0952736).

REFERENCES

1. Traynelis, S. F., L. P. Wollmuth, …, R. Dingledine. 2010. Glutamate receptor ion channels: structure, regulation, and function. *Pharmacol. Rev.* 62:405–496.
2. Benveniste, M., and M. L. Mayer. 1991. Structure-activity analysis of binding kinetics for NMDA receptor competitive antagonists: the influence of conformational restriction. *Br. J. Pharmacol.* 104:207–221.
3. Johnson, J. W., and P. Ascher. 1987. Glycine potentiates the NMDA response in cultured mouse brain neurons. *Nature.* 325:529–531.
4. Clements, J. D., and G. L. Westbrook. 1991. Activation kinetics reveal the number of glutamate and glycine binding sites on the N-methyl-D-aspartate receptor. *Neuron.* 7:605–613.
5. Mayer, M. L., G. L. Westbrook, and P. B. Guthrie. 1984. Voltage-dependent block by Mg^{2+} of NMDA responses in spinal cord neurones. *Nature.* 309:261–263.
6. Nowak, L., P. Bregestovski, …, A. Prochiantz. 1984. Magnesium gates glutamate-activated channels in mouse central neurones. *Nature.* 307:462–465.
7. Paoletti, P., C. Bellone, and Q. Zhou. 2013. NMDA receptor subunit diversity: impact on receptor properties, synaptic plasticity and disease. *Nat. Rev. Neurosci.* 14:383–400.
8. Zhu, S., and P. Paoletti. 2015. Allosteric modulators of NMDA receptors: multiple sites and mechanisms. *Curr. Opin. Pharmacol.* 20:14–23.
9. Hansen, K. B., H. Furukawa, and S. F. Traynelis. 2010. Control of assembly and function of glutamate receptors by the amino-terminal domain. *Mol. Pharmacol.* 78:535–549.
10. Yuan, H., K. B. Hansen, …, S. F. Traynelis. 2009. Control of NMDA receptor function by the NR2 subunit amino-terminal domain. *J. Neurosci.* 29:12045–12058.
11. Gielen, M., B. Siegler Retchless, …, P. Paoletti. 2009. Mechanism of differential control of NMDA receptor activity by NR2 subunits. *Nature.* 459:703–707.
12. Furukawa, H., S. K. Singh, …, E. Gouaux. 2005. Subunit arrangement and function in NMDA receptors. *Nature.* 438:185–192.
13. Sobolevsky, A. I., C. Beck, and L. P. Wollmuth. 2002. Molecular rearrangements of the extracellular vestibule in NMDAR channels during gating. *Neuron.* 33:75–85.
14. Beck, C., L. P. Wollmuth, …, T. Kuner. 1999. NMDAR channel segments forming the extracellular vestibule inferred from the accessibility of substituted cysteines. *Neuron.* 22:559–570.
15. Karakas, E., and H. Furukawa. 2014. Crystal structure of a heterotetrameric NMDA receptor ion channel. *Science.* 344:992–997.
16. Lee, C. H., W. Lü, …, E. Gouaux. 2014. NMDA receptor structures reveal subunit arrangement and pore architecture. *Nature.* 511:191–197.
17. Karakas, E., N. Simorowski, and H. Furukawa. 2011. Subunit arrangement and phenylethanolamine binding in GluN1/GluN2B NMDA receptors. *Nature.* 475:249–253.
18. Karakas, E., N. Simorowski, and H. Furukawa. 2009. Structure of the zinc-bound amino-terminal domain of the NMDA receptor NR2B subunit. *EMBO J.* 28:3910–3920.
19. Zhu, S., R. A. Stein, …, E. Gouaux. 2016. Mechanism of NMDA receptor inhibition and activation. *Cell.* 165:704–714.
20. Tajima, N., E. Karakas, …, H. Furukawa. 2016. Activation of NMDA receptors and the mechanism of inhibition by ifenprodil. *Nature.* 534:63–68.
21. Karplus, M., and J. A. McCammon. 2002. Molecular dynamics simulations of biomolecules. *Nat. Struct. Biol.* 9:646–652.
22. Dai, J., and H. X. Zhou. 2015. Reduced curvature of ligand-binding domain free-energy surface underlies partial agonism at NMDA receptors. *Structure.* 23:228–236.
23. Dai, J., and H. X. Zhou. 2016. Semiclosed conformations of the ligand-binding domains of NMDA receptors during stationary gating. *Biophys. J.* 111:1418–1428.
24. Nury, H., F. Poitevin, …, M. Baaden. 2010. One-microsecond molecular dynamics simulation of channel gating in a nicotinic receptor homologue. *Proc. Natl. Acad. Sci. USA.* 107:6275–6280.
25. Nury, H., C. Van Renterghem, …, P. J. Corringer. 2011. X-ray structures of general anaesthetics bound to a pentameric ligand-gated ion channel. *Nature.* 469:428–431.
26. Zhu, F., and G. Hummer. 2010. Pore opening and closing of a pentameric ligand-gated ion channel. *Proc. Natl. Acad. Sci. USA.* 107:19814–19819.
27. Jensen, M. O., V. Jogini, …, D. E. Shaw. 2012. Mechanism of voltage gating in potassium channels. *Science.* 336:229–233.
28. Wen, H., F. Qin, and W. Zheng. 2016. Toward elucidating the heat activation mechanism of the TRPV1 channel gating by molecular dynamics simulation. *Proteins.* 84:1938–1949.
29. Dai, J., and H. X. Zhou. 2013. An NMDA receptor gating mechanism developed from MD simulations reveals molecular details underlying subunit-specific contributions. *Biophys. J.* 104:2170–2181.
30. Cooper, D. R., D. M. Dolino, …, C. F. Landes. 2015. Conformational transitions in the glycine-bound GluN1 NMDA receptor LBD via single-molecule FRET. *Biophys. J.* 109:66–75.
31. Dolino, D. M., D. Cooper, …, V. Jayaraman. 2015. Structural dynamics of the glycine-binding domain of the N-methyl-D-aspartate receptor. *J. Biol. Chem.* 290:797–804.
32. Dolino, D. M., S. Rezaei Adariani, …, H. Sanabria. 2016. Conformational selection and submillisecond dynamics of the ligand-binding domain of the N-methyl-d-aspartate receptor. *J. Biol. Chem.* 291:16175–16185.
33. Sirrieh, R. E., D. M. MacLean, and V. Jayaraman. 2015. Subtype-dependent N-methyl-D-aspartate receptor amino-terminal domain conformations and modulation by spermine. *J. Biol. Chem.* 290:12812–12820.
34. Sirrieh, R. E., D. M. MacLean, and V. Jayaraman. 2015. A conserved structural mechanism of NMDA receptor inhibition: a comparison of ifenprodil and zinc. *J. Gen. Physiol.* 146:173–181.

35. Klepeis, J. L., K. Lindorff-Larsen, …, D. E. Shaw. 2009. Long-time-scale molecular dynamics simulations of protein structure and function. *Curr. Opin. Struct. Biol.* 19:120–127.

36. Tozzini, V. 2005. Coarse-grained models for proteins. *Curr. Opin. Struct. Biol.* 15:144–150.

37. Tozzini, V. 2010. Minimalist models for proteins: a comparative analysis. *Q. Rev. Biophys.* 43:333–371.

38. Atilgan, A. R., S. R. Durell, …, I. Bahar. 2001. Anisotropy of fluctuation dynamics of proteins with an elastic network model. *Biophys. J.* 80:505–515.

39. Tama, F., and Y. H. Sanejouand. 2001. Conformational change of proteins arising from normal mode calculations. *Protein Eng.* 14:1–6.

40. Zheng, W., and S. Doniach. 2003. A comparative study of motor-protein motions by using a simple elastic-network model. *Proc. Natl. Acad. Sci. USA.* 100:13253–13258.

41. Krebs, W. G., V. Alexandrov, …, M. Gerstein. 2002. Normal mode analysis of macromolecular motions in a database framework: developing mode concentration as a useful classifying statistic. *Proteins.* 48:682–695.

42. Dutta, A., J. Krieger, …, I. Bahar. 2015. Cooperative dynamics of intact AMPA and NMDA glutamate receptors: similarities and subfamily-specific differences. *Structure.* 23:1692–1704.

43. Dutta, A., I. H. Shrivastava, …, I. Bahar. 2012. Comparative dynamics of NMDA- and AMPA-glutamate receptor N-terminal domains. *Structure.* 20:1838–1849.

44. Zheng, W., and A. Auerbach. 2011. Decrypting the sequence of structural events during the gating transition of pentameric ligand-gated ion channels based on an interpolated elastic network model. *PLOS Comput. Biol.* 7:e1001046.

45. Zheng, W. 2015. Toward decrypting the allosteric mechanism of the ryanodine receptor based on coarse-grained structural and dynamic modeling. *Proteins.* 83:2307–2318.

46. Zheng, W., and F. Qin. 2015. A combined coarse-grained and all-atom simulation of TRPV1 channel gating and heat activation. *J. Gen. Physiol.* 145:443–456.

47. Bahar, I., and A. J. Rader. 2005. Coarse-grained normal mode analysis in structural biology. *Curr. Opin. Struct. Biol.* 15:586–592.

48. Tama, F., and C. L. Brooks. 2006. Symmetry, form, and shape: guiding principles for robustness in macromolecular machines. *Annu. Rev. Biophys. Biomol. Struct.* 35:115–133.

49. Guex, N., M. C. Peitsch, and T. Schwede. 2009. Automated comparative protein structure modeling with SWISS-MODEL and Swiss-PdbViewer: a historical perspective. *Electrophoresis.* 30 (*Suppl. 1*):S162–S173.

50. UniProt Consortium. 2015. UniProt: a hub for protein information. *Nucleic Acids Res.* 43:D204–D212.

51. Hinsen, K., A.-J. Petrescu, …, G. R. Kneller. 2000. Harmonicity in slow protein dynamics. *Chem. Phys.* 261:25–37.

52. Lu, M., B. Poon, and J. Ma. 2006. A new method for coarse-grained elastic normal-mode analysis. *J. Chem. Theory Comput.* 2:464–471.

53. Yang, L., G. Song, and R. L. Jernigan. 2009. Protein elastic network models and the ranges of cooperativity. *Proc. Natl. Acad. Sci. USA.* 106:12347–12352.

54. Zheng, W., B. R. Brooks, …, D. Thirumalai. 2005. Network of dynamically important residues in the open/closed transition in polymerases is strongly conserved. *Structure.* 13:565–577.

55. Zheng, W., B. R. Brooks, and D. Thirumalai. 2006. Low-frequency normal modes that describe allosteric transitions in biological nanomachines are robust to sequence variations. *Proc. Natl. Acad. Sci. USA.* 103:7664–7669.

56. Zheng, W., and M. Tekpinar. 2009. Large-scale evaluation of dynamically important residues in proteins predicted by the perturbation analysis of a coarse-grained elastic model. *BMC Struct. Biol.* 9:45.

57. Zheng, W. 2016. Probing the structural dynamics of the SNARE recycling machine based on coarse-grained modeling. *Proteins.* 84:1055–1066.

58. Zheng, W. 2012. Coarse-grained modeling of the structural states and transition underlying the powerstroke of dynein motor domain. *J. Chem. Phys.* 136:155103.

59. Zheng, W. 2011. Accurate flexible fitting of high-resolution protein structures into cryo-electron microscopy maps using coarse-grained pseudo-energy minimization. *Biophys. J.* 100:478–488.

60. Tekpinar, M., and W. Zheng. 2010. Predicting order of conformational changes during protein conformational transitions using an interpolated elastic network model. *Proteins.* 78:2469–2481.

61. Zheng, W. 2010. Multiscale modeling of structural dynamics underlying force generation and product release in actomyosin complex. *Proteins.* 78:638–660.

62. Trabuco, L. G., E. Villa, …, K. Schulten. 2008. Flexible fitting of atomic structures into electron microscopy maps using molecular dynamics. *Structure.* 16:673–683.

63. DiMaio, F., M. D. Tyka, …, D. Baker. 2009. Refinement of protein structures into low-resolution density maps using Rosetta. *J. Mol. Biol.* 392:181–190.

64. Zhu, S., D. Stroebel, …, P. Paoletti. 2013. Allosteric signaling and dynamics of the clamshell-like NMDA receptor GluN1 N-terminal domain. *Nat. Struct. Mol. Biol.* 20:477–485.

65. Hansen, K. B., N. Tajima, …, S. F. Traynelis. 2013. Structural determinants of agonist efficacy at the glutamate binding site of N-methyl-D-aspartate receptors. *Mol. Pharmacol.* 84:114–127.

66. Meyerson, J. R., J. Kumar, …, S. Subramaniam. 2014. Structural mechanism of glutamate receptor activation and desensitization. *Nature.* 514:328–334.

67. Yao, Y., J. Belcher, …, A. Y. Lau. 2013. Conformational analysis of NMDA receptor GluN1, GluN2, and GluN3 ligand-binding domains reveals subtype-specific characteristics. *Structure.* 21:1788–1799.

68. Kussius, C. L., and G. K. Popescu. 2010. NMDA receptors with locked glutamate-binding clefts open with high efficacy. *J. Neurosci.* 30:12474–12479.

69. Murthy, S. E., T. Shogan, …, G. K. Popescu. 2012. Probing the activation sequence of NMDA receptors with Lurcher mutations. *J. Gen. Physiol.* 140:267–277.

70. Sobolevsky, A. I., M. P. Rosconi, and E. Gouaux. 2009. X-ray structure, symmetry and mechanism of an AMPA-subtype glutamate receptor. *Nature.* 462:745–756.

71. Kuner, T., L. P. Wollmuth, …, B. Sakmann. 1996. Structure of the NMDA receptor channel M2 segment inferred from the accessibility of substituted cysteines. *Neuron.* 17:343–352.

72. Borschel, W. F., K. A. Cummings, …, G. K. Popescu. 2015. Kinetic contributions to gating by interactions unique to N-methyl-D-aspartate (NMDA) receptors. *J. Biol. Chem.* 290:26846–26855.

73. Hackos, D. H., P. J. Lupardus, …, J. E. Hanson. 2016. Positive allosteric modulators of GluN2A-containing NMDARs with distinct modes of action and impacts on circuit function. *Neuron.* 89:983–999.

74. Volgraf, M., B. D. Sellers, …, J. B. Schwarz. 2016. Discovery of GluN2A-selective NMDA receptor positive allosteric modulators (PAMs): tuning deactivation kinetics via structure-based design. *J. Med. Chem.* 59:2760–2779.

75. Yi, F., T. C. Mou, …, K. B. Hansen. 2016. Structural basis for negative allosteric modulation of GluN2A-containing NMDA receptors. *Neuron.* 91:1316–1329.

76. Gielen, M., A. Le Goff, …, P. Paoletti. 2008. Structural rearrangements of NR1/NR2A NMDA receptors during allosteric inhibition. *Neuron.* 57:80–93.

77. Dürr, K. L., L. Chen, …, E. Gouaux. 2014. Structure and dynamics of AMPA receptor GluA2 in resting, pre-open, and desensitized states. *Cell.* 158:778–792.

78. Ren, H., Y. Zhao, …, R. W. Peoples. 2012. Interactions among positions in the third and fourth membrane-associated domains at the intersubunit interface of the N-methyl-D-aspartate receptor forming sites of alcohol action. *J. Biol. Chem.* 287:27302–27312.

79. Ren, H., A. K. Salous, …, R. W. Peoples. 2007. Mutations at F637 in the NMDA receptor NR2A subunit M3 domain influence agonist potency, ion channel gating and alcohol action. *Br. J. Pharmacol.* 151:749–757.

80. Ren, H., Y. Honse, …, R. W. Peoples. 2003. A site in the fourth membrane-associated domain of the N-methyl-D-aspartate receptor regulates desensitization and ion channel gating. *J. Biol. Chem.* 278:276–283.

81. Zheng, W., B. R. Brooks, and G. Hummer. 2007. Protein conformational transitions explored by mixed elastic network models. *Proteins.* 69:43–57.

82. Zheng, W., and M. Tekpinar. 2014. Analysis of protein conformational transitions using elastic network model. *Methods Mol. Biol.* 1084:159–172.

83. Zheng, W., and M. Tekpinar. 2012. Structure-based simulations of the translocation mechanism of the hepatitis C virus NS3 helicase along single-stranded nucleic acid. *Biophys. J.* 103:1343–1353.

84. Zheng, W. 2011. Coarse-grained modeling of conformational transitions underlying the processive stepping of myosin V dimer along filamentous actin. *Proteins.* 79:2291–2305.

85. Tekpinar, M., and W. Zheng. 2013. Coarse-grained and all-atom modeling of structural states and transitions in hemoglobin. *Proteins.* 81:240–252.

86. Purohit, P., A. Mitra, and A. Auerbach. 2007. A stepwise mechanism for acetylcholine receptor channel gating. *Nature.* 446:930–933.

87. Kazi, R., J. Dai, …, L. P. Wollmuth. 2014. Mechanical coupling maintains the fidelity of NMDA receptor-mediated currents. *Nat. Neurosci.* 17:914–922.

88. Burnashev, N., and P. Szepetowski. 2015. NMDA receptor subunit mutations in neurodevelopmental disorders. *Curr. Opin. Pharmacol.* 20:73–82.

89. Humphrey, W., A. Dalke, and K. Schulten. 1996. VMD: visual molecular dynamics. *J. Mol. Graph.* 14:33–38.